Temporal variability of the Northern Infrared Aurora of Jupiter as captured by JWST

JGR Space Physics

RESEARCH ARTICLE
10.1029/2025JA034261

Temporal Variability of the Northern Infrared Aurora of Jupiter as Captured by JWST

Henrik Melin[1], Tom S. Stallard[1], James O'Donoghue[2], Luke Moore[3,4], Paola I. Tiranti[1], Katie L. Knowles[1], Thomas K. Greathouse[5], Manuel López-Puertas[6], Matthew J. Rutala[7], Rosie Johnson[8], and Emma Thomas[1]

[1]Department of Mathematics, Physics, and Electrical Engineering, Northumbria University, Newcastle upon Tyne, UK, [2]Department of Meteorology, University of Reading, Reading, UK, [3]Department of Astronomy, Boston University, Boston, MA, USA, [4]Center for Space Physics, Boston University, Boston, MA, USA, [5]Southwest Research Institute, San Antonio, TX, USA, [6]Instituto de Astrofísica de Andalucía, CSIC, Granada, Spain, [7]School of Cosmic Physics - Astronomy & Astrophysics, Dublin Institute for Advanced Studies, Dunsink Observatory, Dublin, Ireland, [8]Department of Physics, Aberystwyth University, Aberystwyth, UK

Key Points:

- High fidelity James Webb Space Telescope maps of Jupiter's northern polar ionosphere reveal small scale structures in temperature and ion density
- Auroral ionospheric temperature and density vary significantly over short timescales
- The observed temporal variability is likely linked to short-term changes in the electron precipitation flux and energy

Supporting Information:

Supporting Information may be found in the online version of this article.

Correspondence to:

H. Melin,
henrik.melin@northumbria.ac.uk

Citation:

Melin, H., Stallard, T. S., O'Donoghue, J., Moore, L., Tiranti, P. I., Knowles, K. L., et al. (2025). Temporal variability of the northern infrared aurora of Jupiter as captured by JWST. *Journal of Geophysical Research: Space Physics*, *130*, e2025JA034261. https://doi.org/10.1029/2025JA034261

Received 3 JUN 2025
Accepted 13 AUG 2025

Author Contributions:

Conceptualization: Henrik Melin, Tom S. Stallard
Data curation: Tom S. Stallard, Thomas K. Greathouse, Manuel López-Puertas
Formal analysis: James O'Donoghue, Luke Moore
Investigation: James O'Donoghue, Paola I. Tiranti, Katie L. Knowles, Matthew J. Rutala
Methodology: Henrik Melin
Validation: Katie L. Knowles, Emma Thomas
Visualization: Henrik Melin, Thomas K. Greathouse
Writing – original draft: Henrik Melin, Luke Moore

Abstract We present near-infrared observations of the northern aurora of Jupiter using the NIRSpec instrument on the James Webb Space Telescope, mapping emissions from H_3^+ and CH_4 across the polar region. The data were acquired over a period of ~4 hr, providing a temporally averaged view of these emissions. From the H_3^+ spectra we derive the temperature of the upper atmosphere and H_3^+ ion densities. Temperatures are elevated along the main auroral oval at both dawn and dusk, though the highest temperatures recorded were poleward of the main oval at dawn, approaching 1500 K. The highest ion densities were observed dusk-ward of the main oval, closely correlating with the observed H_3^+ radiance. Using overlapping individual observations (or dithers) we investigate the temporal variability of the temperatures, which we found change too fast to represent wholesale changes to the vertical temperature structure of the upper atmosphere. Instead, these fast changes are likely connected to variable electron precipitation energies, which produce H_3^+ at different altitudes that sample different parts of the thermospheric temperature profile. The 3.3 μm CH_4 fundamental and hotband emissions are brightest at 210°W close to the pole, which has been seen previously. However, we also see emission along the main oval, suggesting excitation of this non-LTE emission by direct precipitation. Lastly, we suggest that the CH_4 band ratios can be used to trace the penetration depth of the precipitating electrons, and therefore their energies.

Plain Language Summary The James Webb Space Telescope is the most advanced telescope ever constructed and it provides unrivaled sensitivity with which to observe our Universe. By pointing the telescope at Jupiter's northern pole we can observe the bright northern lights, or aurora, of the planet. These vibrant light-shows are a result of the charged particles streaming along magnetic field-lines, crashing into the upper atmosphere, causing both excitation and ionization. An important signature of this process are the emissions from the molecular ion H_3^+ and by observing its near-infrared spectrum, we can derive the ion's temperature and density, which are tracers of thermal and chemical change in the auroral region. Because the observations overlap on the planet, we can investigate how the temperature and density change over time. These changes are very large and fast, which suggests that the electrons responsible for creating H_3^+ are changing energy rapidly.

1. Introduction

The bright aurora of Jupiter is produced by the most vociferous interaction between neutral thermosphere, charged particle ionosphere, and magnetosphere within our Solar System. Vast current-systems, largely driven by the motions of plasma within the magnetosphere (e.g., Cowley & Bunce, 2001) and by wave particle interactions above the atmosphere (e.g., Sulaiman et al., 2022), are established that flow into and through the planet's ionosphere. Collisions between charged particles and the neutral atmosphere generate significant heating in this region, via electron impact, Joule heating, and ion drag (e.g., Lystrup et al., 2007; Tao et al., 2009; Wang et al., 2024). As the currents travel into, out, and through the atmosphere they also excite and ionize its constituents, producing emission at different wavelengths, from X-ray to radio (see Badman et al., 2015; Yelle & Miller, 2004). These different emissions provide unique information about the energetics and dynamics of the auroral process, and how it alters the physical state of the atmosphere.

Writing – review & editing: Henrik Melin, James O'Donoghue, Luke Moore, Paola I. Tiranti, Katie L. Knowles, Thomas K. Greathouse, Manuel López-Puertas, Matthew J. Rutala, Rosie Johnson, Emma Thomas

The ionosphere is the charged component of the upper atmosphere, and a major constituent within it is the molecular ion H_3^+, along with H^+. By performing remote sensing spectroscopic observations of H_3^+ in the near-infrared, the physical properties of this region can be determined (e.g., Miller et al., 2020), namely: temperature, H_3^+ column density, and radiative cooling rates. The retrieved H_3^+ temperature is a column average, weighted by the H_3^+ density altitude profile, so the derived temperature is biased toward the lower part of the ionosphere where it is densest (Moore et al., 2019). In other words, spatial or temporal changes in the observed H_3^+ temperature can be interpreted in two ways: (a) changes in the heating and cooling of the upper atmosphere due to internal (e.g., deposition of gravity waves) and external forcing (magnetospheric processes) and/or (b) changes in the precipitating electron energy and flux, producing H_3^+ at different altitudes, sampling different parts of the increasing (in altitude) temperature profile (e.g., Grodent et al., 2001; Seiff et al., 1996; Tao et al., 2011).

In the auroral region, the main mechanism of H_3^+ production is via electron impact ionization of H_2, and the energy distribution of the electrons will determine at what altitude H_3^+ is produced. For example, low energy (soft) electrons will produce H_3^+ at high altitudes, whereas high energy (hard) electrons will produce H_3^+ at lower altitudes. If the altitude of maximum energy deposition is below the homopause (<20 keV, Tao et al., 2011), the precipitating electrons will not increase the density of H_3^+. This is because the ion is rapidly destroyed via charge exchange by molecular species that have a proton affinity higher than H_2, that is, by hydrocarbons such as methane (CH_4).

The northern H_3^+ aurora has been spectroscopically mapped by both ground-based and spacecraft instrumentation (Dinelli et al., 2017; Johnson et al., 2018; Lam et al., 1997; Moore et al., 2017; Nichols et al., 2025; O'Donoghue et al., 2021; Raynaud et al., 2004; Stallard et al., 2002; Wang et al., 2023). These types of observations reveal the northern aurora to be hundreds of K hotter than lower and equatorial latitudes, with a relatively smooth temperature gradient from pole-to-pole (e.g., O'Donoghue et al., 2021; Roberts et al., 2025).

Johnson et al. (2018) observed the H_3^+ morphology and temperature distribution of the northern aurora using the Very Large Telescope, with the combination of an 8 m telescope and $R = 100{,}000$ spectrometer providing the lowest uncertainty temperature measurements to date. Whilst the dawn emission were spatially confined, they coincided with a broad region of elevated temperature (~950 K). This is in contrast to the dusk region, which was brighter across a range of longitudes, but was much cooler than dawn (~850 K). Of particular note is a warm region that traversed the auroral region, from dusk to dawn, elevated by about 50 K. Moore et al. (2017) produced temperature maps with similar temperature structures. Juno JIRAM observed the opposite scenario, wherein the dusk main oval was warmer by about 100 K, compared to the dawn oval (Dinelli et al., 2017), indicating that the morphology of the auroral temperatures can change significantly between different epochs. Wang et al. (2024) observed the northern aurora of Jupiter using the Keck telescope, with partial coverage, and found elevated temperatures at dawn and dusk, along the main oval up to 1050 K. They concluded that the bulk of the auroral heating occurs at altitudes below the peak H_3^+ production.

Precipitating electrons can directly excite H_2 to produce emission observable in the ultraviolet and more energetic electrons can enhance deeper CH_4 emissions (1–10 μbar, Sinclair et al., 2019). The CH_4 emissions have a very different morphology to that of H_2 and H_3^+, dominated by an extended bright region, appearing at high latitudes within the northern edge of the main oval with a temperature of ~500 K (Kim et al., 2015; Moriconi et al., 2017). While the exact driver of the CH_4 emission is not known it is thought to result from one or more of the following: (a) increased temperatures, e.g., by auroral heating near the homopause (b) elevated homopause altitudes (Sánchez-López et al., 2022), and, (c) non-LTE effects that pump the CH_4 energy states (Sinclair et al., 2019), and (d) direction excitation of vibrational states by electrons (Bhardwaj & Mukundan, 2015).

The James Webb Space Telescope (JWST), with its unrivaled infrared sensitivity, provides an opportunity to shed new light on Jupiter's auroral region, and how magnetospheric interactions affects the upper atmosphere. Here, we present JWST NIRSpec Integral Field Unit (IFU) observations of the northern aurora. In Section 2, we describe the observations and analysis process, followed by a description of results in Section 3 and a discussion in Section 4, and finishing with a summary in Section 5.

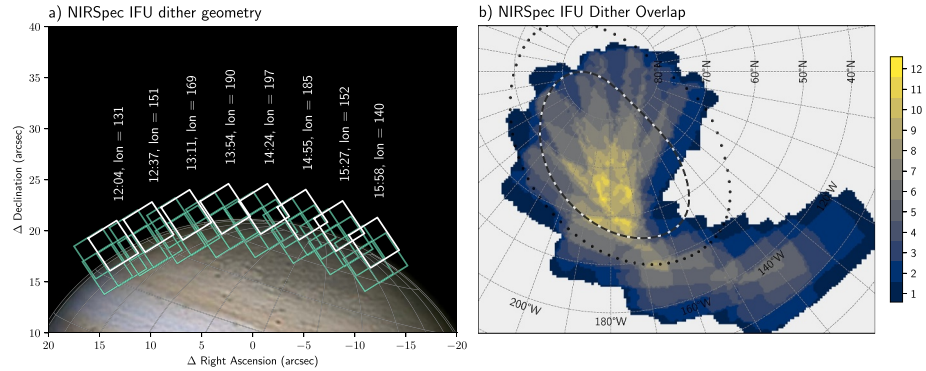

Figure 1. (a) Geometry of the JWST NIRSpec IFU observations on 2023-09-07, showing the first dither of an observation in white (with mid-observation UTC time and median System III longitude indicated), and the other dithers in green. The background image (for context) was obtained on 2023-09-08 03:06 UTC by Yann Le Gall in France. The RA and Dec coordinates are relative to the center of the planet. (b) The projected overlap of the 32 individual dithers. The dashed white line indicates the expected location of the main auroral oval (30 R_J, Connerney et al., 2022), and the dotted lines shows the magnetic mapping of the orbit of Io (5.9 R_J). Dawn is to the left, and dusk is to the right.

2. Observations and Data Analysis

The observations presented here are part of JWST program #3665 (Principal Investigators T. S. Stallard and H. Melin), which scanned the limb of Jupiter using the NIRSpec IFU (Jakobsen et al., 2022), starting at 35°N on the dawn side scanning clock-wise around the planet. The primary aim of the program was to directly observe vertical ionospheric profiles as a function of latitude at both dusk and dawn, and occurred at the same time as a Juno radio occultation during perijove 54 (PJ54). The F290LP/G395H filter/disperser was used, producing spectral cubes between 2.87 and 5.14 μm, at a spectral resolution of R∼2,700. Each spaxel has a spatial resolution of $0.1'' \times 0.1''$ and the IFU comprises 30 × 30 spaxels. The first eight observations, each with 4 dithers, executed as expected, but during the subsequent observation the guide-star acquisition failed, and no further data from Jupiter was obtained until later in the day. The exposure time per dither is 86 s (4 groups and one exposure using the NRSRAPID readout mode), and the JWST calibration context was `jwst_1237.pmap`. Each dither was processed separately to Calibration Level 3, using the `ifualign` coordinate system and the `emsm` weighting in the `cube_build` step, to reduce the effect of fringing.

The observational geometry was calculated using the `JWSTSolarSystemPointing` Python class, which uses pointing information from the JWST World Coordinate System (WCS) and NASA's Navigation and Ancillary Information Facility (NAIF, Acton, 1996). The mean emission angles and local-times are shown in Figure S1 in Supporting Information S1. Figure 1a shows the observational geometry of the observations, obtained on 2023-09-07, with details listed in Table 1. As the scan moves from left to right, Jupiter rotates underneath, so a significant portion of the northern aurora (centered at about 180°W) was captured. Figure 1b shows the projected overlap of individual dithers, with a maximum overlap of 12 dithers, highlighting that most of the northern auroral region is captured by this (intentional) observational design.

The wavelength region between 3.2 and 4.1 μm contains strong absorption of sunlight by deep CH_4 that produces a spectral region void of solar reflectance features from the lower atmosphere, and bright H_3^+ and high altitude non-LTE CH_4 emission lines are seen. Here, the modeling of the non-LTE CH_4 emissions is highly simplified, as the full treatment is very complex and falls outside the scope of this study. This simplified process is outlined in Melin et al. (2024), and involves modeling the CH_4 spectrum with three basic components: a fundamental spectrum ($\nu_3 \rightarrow$ ground), a hotband component ($\nu_3 + \nu_4 \rightarrow \nu_3$), and a polynomial background. Whilst this approach does not yield CH_4 temperature and density, it allows us to extract both the fundamental and hotband radiances from the JWST observations. Once the CH_4 and background components have been quantified, they can be subtracted to reveal the isolated H_3^+ spectrum. Figure 2a (top) shows an example spectrum from an individual IFU spaxel, showing the CH_4 (fundamental and hotband) and the H_3^+ model components required to fit the data, as well as the residual spectral radiance (bottom). The residual falls largely within the 3-σ uncertainty, which is based on the instrumental Poisson and read noise.

Table 1
The JWST NIRSpec IFU Observations Used in This Study, Obtained on 2023-09-07, Showing the Observation Name, Dither Number, the Mid-Time of the Observation, the Median Latitude, System III West Longitude, and Local-Time

Observation name	Dither	Time (UTC)	Lat (°)	Lon (°)	LT (h)
1 JUPITER-DAWN-L35N	1	12:04:42	36.4	131.3	7.6
2 JUPITER-DAWN-L35N	2	12:08:17	31.0	125.7	8.2
3 JUPITER-DAWN-L35N	3	12:11:52	32.7	136.9	7.6
4 JUPITER-DAWN-L35N	4	12:15:26	34.7	128.7	8.3
5 JUPITER-DAWN-L45N	1	12:37:59	45.7	150.6	7.7
6 JUPITER-DAWN-L45N	2	12:41:34	40.2	142.4	8.4
7 JUPITER-DAWN-L45N	3	12:45:09	41.8	154.4	7.7
8 JUPITER-DAWN-L45N	4	12:48:43	44.2	145.8	8.5
9 JUPITER-DAWN-L55N	1	13:11:27	54.9	169.3	7.8
10 JUPITER-DAWN-L55N	2	13:15:02	49.2	157.3	8.7
11 JUPITER-DAWN-L55N	3	13:18:37	50.9	170.8	8.0
12 JUPITER-DAWN-L55N	4	13:22:11	53.6	161.6	8.8
13 JUPITER-DAWN-L65N	1	13:54:02	63.8	190.2	8.1
14 JUPITER-DAWN-L65N	2	13:57:37	57.7	175.0	9.3
15 JUPITER-DAWN-L65N	3	14:01:12	59.6	190.2	8.4
16 JUPITER-DAWN-L65N	4	14:04:47	62.5	179.6	9.3
17 JUPITER-DAWN-L75N	1	14:24:49	72.3	197.0	8.9
18 JUPITER-DAWN-L75N	2	14:28:24	65.0	179.6	10.2
19 JUPITER-DAWN-L75N	3	14:31:59	67.8	197.3	9.2
20 JUPITER-DAWN-L75N	4	14:35:33	70.6	183.3	10.3
21 JUPITER-DAWN-L85N	1	14:55:57	79.3	185.1	11.0
22 JUPITER-DAWN-L85N	2	14:59:32	69.6	175.7	11.7
23 JUPITER-DAWN-L85N	3	15:03:07	74.4	192.4	10.8
24 JUPITER-DAWN-L85N	4	15:06:42	75.8	172.0	12.3
25 JUPITER-DUSK-L85N	1	15:27:16	79.6	152.2	14.4
26 JUPITER-DUSK-L85N	2	15:30:51	69.6	166.3	13.6
27 JUPITER-DUSK-L85N	3	15:34:26	76.1	176.0	13.1
28 JUPITER-DUSK-L85N	4	15:38:01	74.5	156.4	14.6
29 JUPITER-DUSK-L75N	1	15:58:46	72.7	139.9	16.5
30 JUPITER-DUSK-L75N	2	16:02:21	65.2	162.4	15.2
31 JUPITER-DUSK-L75N	3	16:05:56	71.2	165.4	15.1
32 JUPITER-DUSK-L75N	4	16:09:30	67.9	151.6	16.2

Since there is significant overlap of the individual dithers in the auroral region (Figure 1b), we construct a median spectrum for each point on a projected grid in the following way:

1. The modeling procedure outlined above was applied to each spaxel of each dither to produce the isolated H_3^+ spectrum, as well as the CH_4 fundamental and hotband components, each to be projected separately.
2. Each wavelength slice of each dither was projected onto a System III (Seidelmann & Divine, 1977) planetocentric latitude and west longitude grid with $0.2° \times 0.2°$ resolution. Both the optically thin H_3^+ emissions and optically thick CH_4 emissions are highly dependent on the observing geometry, and both increase sharply toward the limb as the line-of-sight column length increases. In order to combine the individual JWST observations, each with slightly different observing geometry, we apply a correction factor at each spaxel to account for this. For the H_3^+ emissions we apply a simple line-of-sight correction, assuming a uniform slab of 500 km (Johnson et al., 2018). For the CH_4 emissions, the dependence on emission angle was analytically

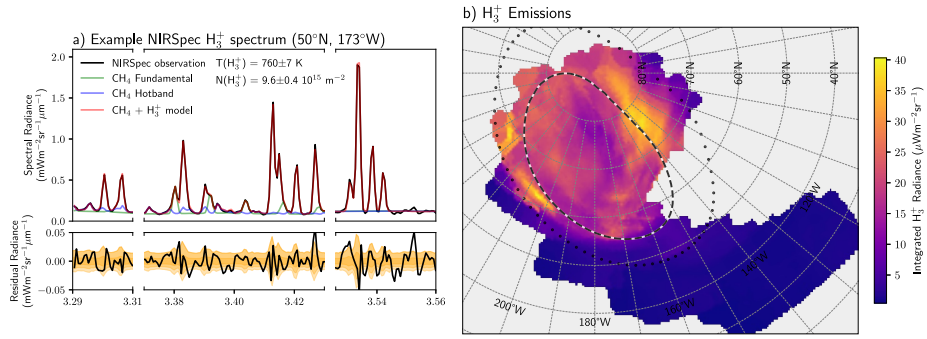

Figure 2. (a) An example JWST NIRSpec IFU spectrum (top), showing the CH_4 fundamental, CH_4 hotband, and H_3^+ components required to model the observed spectrum. The bottom plot shows the residuals of the data fitting procedure, with the shaded region indicating the 3-σ uncertainty. (b) The projected map of Jupiter's northern H_3^+ aurora derived from the JWST NIRSpec IFU observations.

characterized away from the auroral region, at the dawn equator, where solar processes dominate. Figure 3a shows the integrated radiance as a function of emission angle, and a quadratic function was fitted (R_{CH_4}):

$$R_{CH_4}(\theta) = a_1 + a_2\theta + a_3\theta^2 \tag{1}$$

where θ is the emission angle and the a_n are the polynomial constants. For the fundamental band, the constants are $a_n = (1.30 \times 10^{-2}, -3.27 \times 10^{-4}, 2.84 \times 10^{-6})$, and for the hotband they are $a_n = (2.12 \times 10^{-2}, -6.37 \times 10^{-4}, 5.40 \times 10^{-6})$. The geometric correction factor for a particular emission angle, $C_{CH_4}(\theta)$, was then constructed as follows:

$$C_{CH_4}(\theta) = \frac{R_{CH_4}(60°)}{R_{CH_4}(\theta)} \tag{2}$$

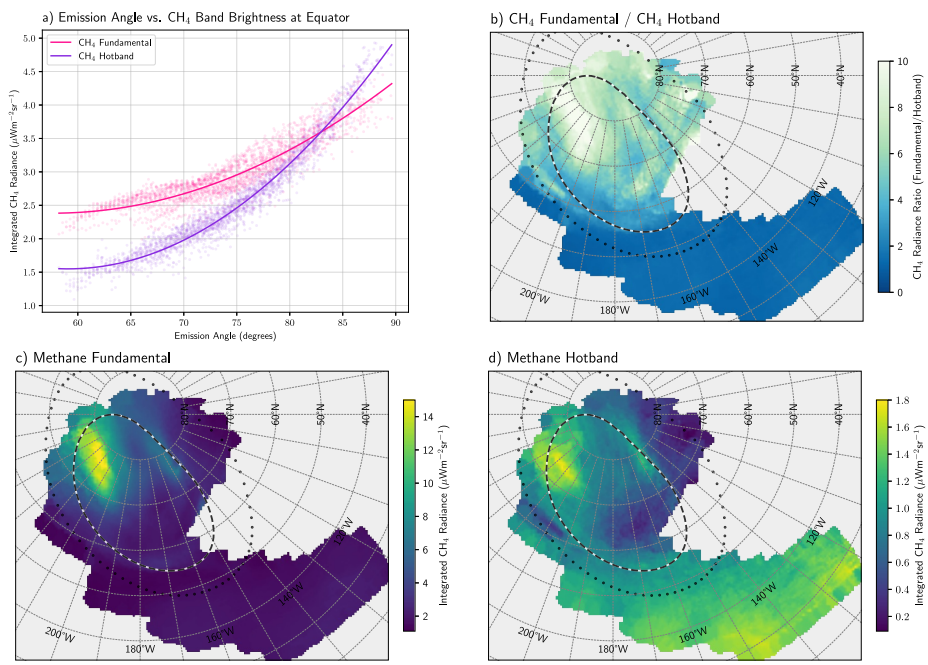

Figure 3. (a) The integrated CH_4 fundamental and hotband radiances on the dawn equator (dots). The quadratic fits (solid lines) are used to derive a geometric correction factor for the CH_4 emissions at the pole. (b) The ratio between the CH_4 fundamental and hotband emissions (c) The CH_4 fundamental emission (d) The CH_4 hotband emission.

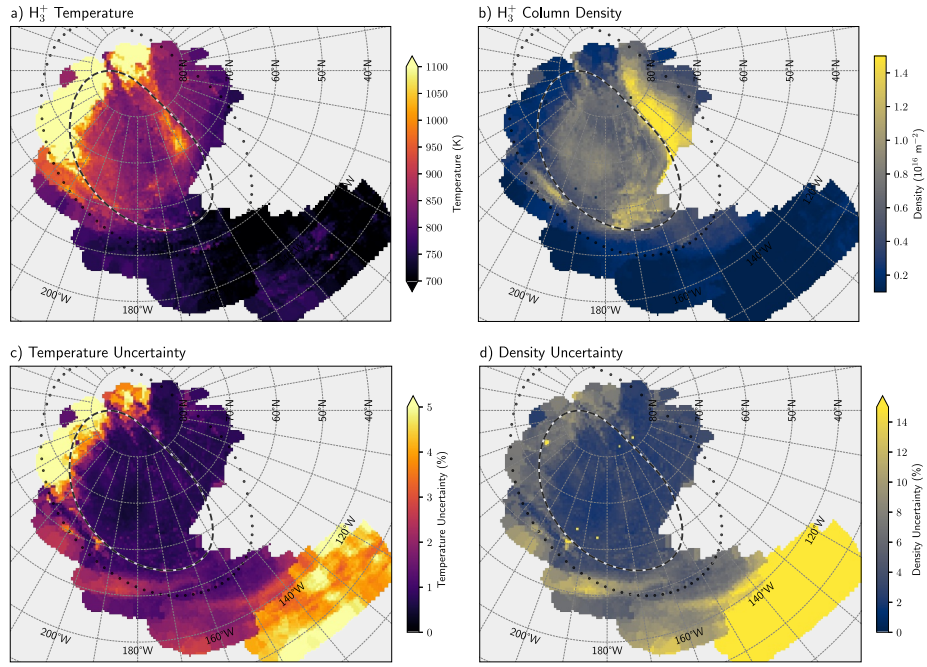

Figure 4. (a) The polar projected retrieved H_3^+ temperatures using `h3ppy`. The plot is limited to 1100 K, but they extend up to ~1500 K in the high-latitude dawn region. (b) The retrieved H_3^+ column integrated densities. (c) The percentage uncertainty in the temperature, and the (d) percentage uncertainty in the H_3^+ column density.

The H_3^+ emissions were projected to an altitude of 550 km above the 1-bar pressure level (Grodent et al., 2001), and the CH_4 emissions were projected to an altitude of 250 km. In the NAIF system, the 1-bar pressure "surface" of Jupiter is defined by the oblate spheroid described by an equatorial radius of 71,492 km and a polar radius of 66,854 km.

3. For each wavelength in the spectral region of interest (Figure 2a), the spectral radiance was calculated by taking the median of the projected dithers at that wavelength, which overlap on the projected grid. In this manner, we produced projected median spectra for H_3^+ and the CH_4 fundamental and hotband emissions.

Figure 2b shows the integrated H_3^+ radiance in the auroral region, where the dashed line indicates a L-shell of 30 R_J, the expected location of the main auroral oval (Connerney et al., 2022) and the dotted lines shows the magnetically mapped orbit of Io at 5.9 R_J. The radiance integrated CH_4 fundamental component is shown in Figure 3c, and the CH_4 hotband is shown in Figure 3d and the ratio between the CH_4 fundamental to the hotband radiances is shown in Figure 3b.

By fitting the projected H_3^+ spectrum at each latitude and longitude using the *h3ppy* fitting code (Melin, 2025b), maps of H_3^+ temperature (T) and column integrated density (N) can be produced across Jupiter's polar region, along with their uncertainties, assuming conditions of quasi-Local Thermal Equilibrium (LTE, Johnson et al., 2018). These are shown in Figures 4a and 4b, with the uncertainties shown in Figures 4c and 4d. The increased uncertainties toward lower latitudes is driven by a decrease in the signal-to-noise.

Figure 1b shows the spatial overlap between individual IFU dithers. Where the same region on the planet is covered by two or more dithers, the temporal variability of the H_3^+ temperature and density can be investigated. To facilitate this, the CH_4 and background subtracted spectra of each individual dither was fitted using *h3ppy*, and the retrieved temperature and H_3^+ column density along with their uncertainties, where projected in the same style as Figure 4. This produced 32 maps of H_3^+ temperature and H_3^+ column density, all with different latitude and longitude coverage. Figure 5a shows the maximum difference in time for overlapping observations in seconds, that is, the latest minus the earliest time for the overlap of the dithers across the pole ($t_{max} - t_{min}$). The longest time difference occurs where the greatest spatial overlap is located (2.9 hr), whereas fewer overlapping dithers yields shorter timespans. This indicates the timespan during which any changes are captured. Figure 5b shows the

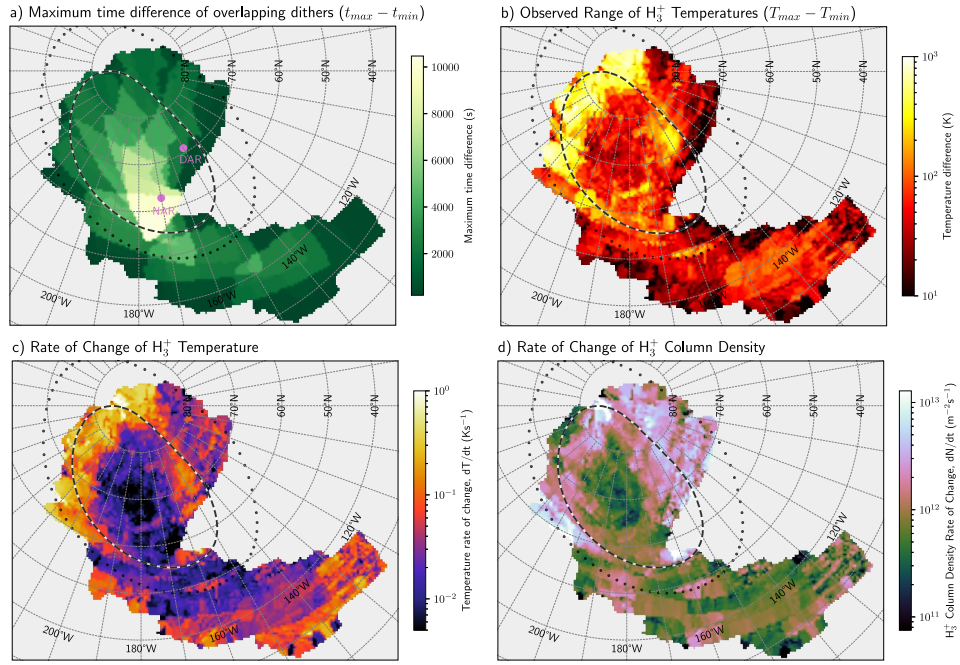

Figure 5. (a) The maximum time difference between spatially overlapping IFU dithers on 2024-09-07. The dots shows the locations of the NAR and DAR, shown in more detail in Figure 6. (b) The maximum difference in temperature retrieved from individual overlapping dithers. (c) The temperature rate of change (dT/dt), calculated from Equation 3, and (d) the density rate of change (dN/dt), calculated from Equation 4.

difference between the largest and smallest retrieved temperature ($T_{\max} - T_{\min}$), showing the change in temperature over the periods indicated in Figure 5a. By dividing the magnitude of the change temperature and H_3^+ density by the timescales (i.e., by Figure 5a), we produce the average rate of change of these parameters over the sampled time period, which can be expressed as:

$$\frac{dT}{dt} = \frac{\Delta T}{\Delta t} = \frac{T_{\max} - T_{\min}}{t_{\max} - t_{\min}} \tag{3}$$

and

$$\frac{dN}{dt} = \frac{\Delta N}{\Delta t} = \frac{N_{\max} - N_{\min}}{t_{\max} - t_{\min}} \tag{4}$$

These are shown in Figures 5c and 5d, respectively. These rate-of-change parameters provide a direct measure of the variability of the H_3^+ temperature and density, in Jupiter's northern auroral region, as captured by these JWST observations. This should be considered as the minimum rate of change since, for example, T_{max} and T_{min} at a particular longitude and latitude may not be contained in the first and the last of overlapping dithers.

The detailed temporal variability can be investigated at any point where dithers overlap. Here, we investigate two regions of interest: the "noon active region" (NAR, ~63°N/170°W) and the "dusk active region" (DAR, ~71°N/150°W, Nichols et al., 2009), and the temporal evolution of H_3^+ temperature (black) and column density (red) at these points is shown in Figure 6. The location of these two points are indicated as annotated dots in Figure 5a. The NAR region (Figure 6a) has the largest number of overlapping dithers (12—see Figure 1a), whereas the DAR region (Figure 6b) has six overlapping dithers.

2.1. Juno UVS

The Ultraviolet Spectrograph (Gladstone et al., 2017) onboard the Juno spacecraft has spectral coverage between 68 and 210 nm, covering the H_2 Lyman and Werner band auroral emissions. During PJ54, the orbital geometry

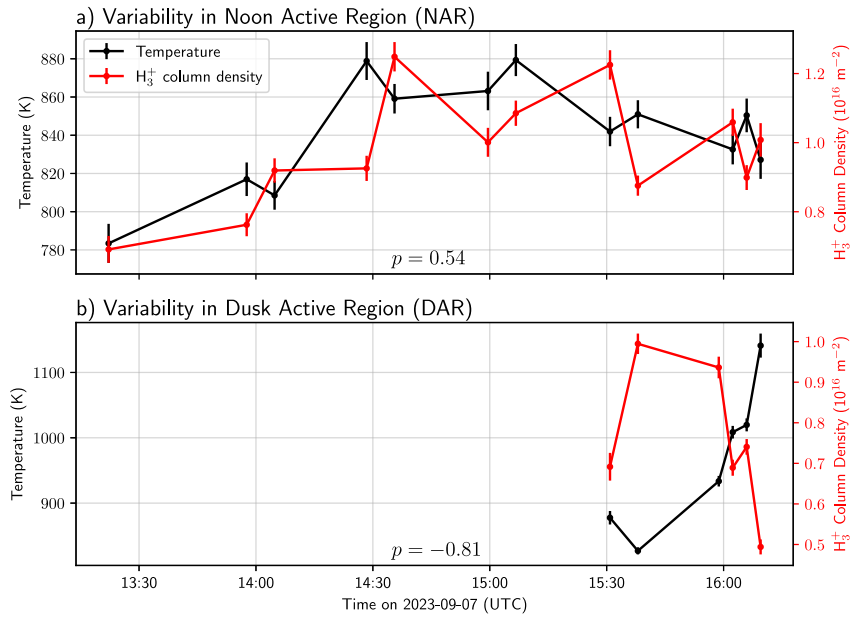

Figure 6. The temporal evolution of H_3^+ temperature and column density at the (a) "noon active region" (NAR) and (b) the "dusk active region" (DAR). These regions are indicated as dots in Figure 5a. The Pearson correlation coefficient between the temperature and density for each region is indicated (p).

was not favorable for observations of Jupiter's northern aurora, and it could only be observed at high emission angles. Nonetheless, we consider observations obtained between 11:36 and 11:43 on 2023-09-07 that provide partial coverage of the northern pole, acquired just before the start of the JWST observations. The data was processed in the same way as Greathouse et al. (2021). The H_2 brightness between 155 and 162 nm is shown in Figure 7a, and the H_2 color ratio (i.e., 155–162 nm divided by 123–130 nm) can be seen in Figure 7b.

We note that the Jovian Infrared Auroral Mapper (JIRAM; Adriani et al., 2017) would have provided a highly complementary data set to the JWST observations, with overlapping near-infrared spectral coverage. However, during PJ54, the spatial coverage of JIRAM in the northern auroral region was insufficient to enable a meaningful comparison.

3. Results

The H_3^+ map of northern auroral emission (Figure 2b) represents a median view over ∼4 hr of observation, covering local-times between ∼7 and ∼16 *h* (Table 1). The main auroral emissions are narrowly confined at dawn

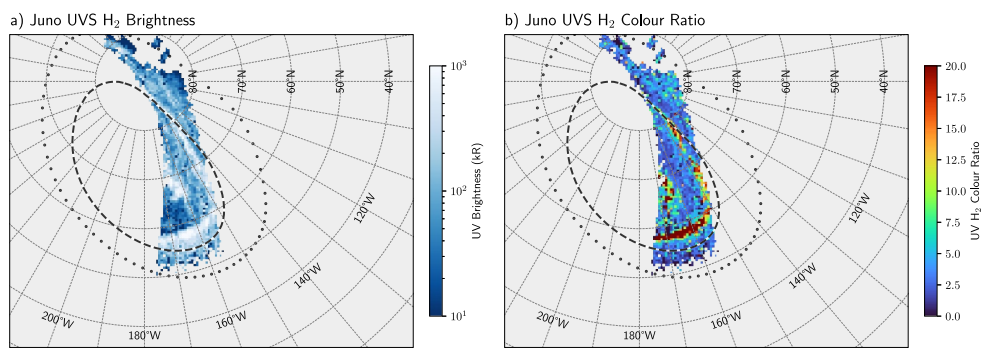

Figure 7. (a) The Juno UVS observations of Jupiter's aurora during PJ54 obtained between 11:36 and 11:43 on 2023-09-07, just before the JWST auroral observations, showing the total brightness of H_2 between 155 and 162 nm. (b) The UV color ratio, that is, 155–162 nm divided by 123–130 nm. High ratios are indicative of energetic electrons penetrating down to low altitudes.

but broader across the dusk region. There are bright and spatially variable polar emissions, including a number of small scale features, seen at the NAR and the DAR. The "dark region", just inside the dawn oval appears dark, as does an extended dark region centered at ~75°N/170°W. The observed lower latitude H_3^+ emissions are ~10% of the auroral emissions.

Figure 4 shows the projected H_3^+ temperatures and column integrated densities, along with uncertainty for each parameter. The range of observed temperatures is large, from ~700 up to ~1500 K, whereas the plot is thresholded to 1100 K to more clearly show the spatial variability across the aurora. The high latitude dawn region is by far the hottest, but localized heating is also observed along the lower latitude dawn oval as well. At dusk, there is an extended region of elevated temperatures located inside the main auroral oval (DAR), with localized regions of higher temperatures seen at the NAR. The "dark region" does not show any decrease in temperature, and is instead rendered dark by lower H_3^+ column densities. The median temperature across the entire field of view is 862 K with a standard deviation of 223 K, whereas the median temperature at latitudes above 55°N is 897 K, with a standard deviation of 219 K.

The H_3^+ column densities in Figure 4 are morphologically similar to the integrated H_3^+ radiance (Figure 2b), with a Pearson correlation coefficient of $p = 0.65$ between the two. The column densities peak dusk-ward of the main oval at $\sim 1.5 \times 10^{16}$ m^{-2}, and the median density across the entire field-of-view is 5.2×10^{15} m^{-2}, with a standard deviation of 3.5×10^{15} m^{-2}. There is no strong anti-correlation between the retrieved H_3^+ temperatures and densities ($p = -0.27$), highlighting the excellent signal-to-noise ratios of the data (Melin et al., 2014) which results in small uncertainties (Figures 4c and 4d).

Figure 5c shows the observed minimum rate of change in temperature. The largest temperature changes occurs on the dawn edge of the main oval, close to the pole (~ 1Ks^{-1}), and there are pronounced changes occurring at 73°N/150°W (at the DAR), and along the dusk edge of the auroral oval. The smallest temperature changes occur at the center of the auroral oval, and equatorward of the main oval. The variability along the Io footprint aurora is explored in a parallel study. The variability observed at low latitudes is of note, and this is a region associated with significant uncertainties (see Figure 4c), due to lower signal-to-noise ratios. However, the observed difference in temperature is above the retrieved uncertainties, and so this may be considered to be real.

The rate of change of the H_3^+ column density is shown in Figure 5d, with changes of up to $\sim 10^{13}$ m^{-2}s^{-1}, particularly on the dusk oval, extending down toward lower L-shells (to the right). Very low variability is observed at the center of the oval, which increases toward the oval itself. The variability at lower latitudes appears stochastic.

Figures 3c and 3d shows the corrected (Equation 2) and projected 3.3 μm CH_4 fundamental and hotband emissions with a distinct brightening around 210°W inside the main auroral oval (dashed lines), and weaker emissions along most of the main auroral oval. For the hotband, stronger emissions are present at lower latitudes, where the solar incidence angle is smaller, generating stronger fluorescence. The ratio between the CH_4 fundamental and hotband emission is shown in Figure 3b, and highlights that the two components do not have the same morphology, with significant differences across the auroral region. For example, along the main oval the hotband is brighter (i.e., the ratio is lower) than at the bright emission at 210°W, where the fundamental emissions are brighter.

The temporal evolution of the NAR and DAR is shown in Figure 6, and the two exhibit very different behaviors. In the NAR, both the H_3^+ temperature and column density appears to vary in unison and as the temperature increases so does the column density, with a Pearson correlation coefficient of $p = 0.54$. The temperature changes overall are relatively small, ~12%, whereas the changes in column density are much larger, ~81%. The fastest change in temperature occurs between 16:02 and 16:06 with a difference of 18 K, which equates to 0.08 Ks^{-1}. The fastest change in H_3^+ column density occurs between 14:48 and 14:35 with a difference of 0.3×10^{16} m^{-2}, which equals a rate of change of 7.5×10^{12} m^{-2}s^{-1}. In the DAR, where the dither overlap is smaller, the temperature and column density appear strongly anti-correlated ($p = -0.81$), and the variability in both temperature and column density is large, ~38% and ~101%, respectively. The fastest change in temperature occurs between 16:06 and 16:10 with a difference of 121 K, which gives a rate of change of 0.6 Ks^{-1}. The fastest change in H_3^+ column density occurs between 15:31 and 15:38 with a difference of 0.3×10^{16} m^{-2}, which equals a rate of change of 7.1×10^{12} m^{-2}s^{-1}, which is very similar to what is observed at the NAR.

The ultraviolet Juno UVS observations of the H_2 brightness, obtained slightly before the JWST auroral observations, are shown in Figure 7a, and the derived color ratio is shown in Figure 7b. Whilst the slant viewing geometry from the spacecraft affords a relatively patchy view, clear emissions are observed along the main oval, as well as within it. The higher color ratios along the main oval, as well as within it (at the NAR), indicate more energetic precipitation at those locations.

4. Discussion

The temporally averaged morphology of the H_3^+ auroral emissions in Figure 2b share similarities with previous studies: bright emission along the main auroral oval, and significant levels of emissions contained within the main oval, with a number small-scale structures situated within it (Gérard et al., 2018; Johnson et al., 2018) at the NAR and DAR.

The H_3^+ temperature retrievals in Figure 4a reveal the fine-scale structure of the auroral heating at the H_3^+ altitudes. The range of temperatures observed here (~500–1500 K) is much larger than observed with Juno JIRAM during the first perijove (700–950 K, Dinelli et al., 2017), and the spatial distributions also show significant differences. First, the very high temperatures at high latitudes at dawn in Figure 4a are not seen in the JIRAM observations. Second, the Dinelli et al. (2017) temperatures at dusk peak outside of the main oval, whilst the density peaks inside it. Here we see the opposite, with temperatures peaking at ~1000 K inside the main oval, whilst the densities have a broad distribution just outside of it (Figure 4b). Third, the peak densities of Dinelli et al. (2017) are observed at dawn, whilst the peak densities here are seen at dusk. This highlights the strong variability of Jupiter's aurorae.

Previous ground-based observations have also produced high-fidelity maps of H_3^+ temperature and column density (Johnson et al., 2018; Moore et al., 2017; O'Donoghue et al., 2021; Raynaud et al., 2004; Wang et al., 2024). Again, the range of temperatures found in those studies is less (~600–1000 K) than observed here. This may be related to the fact that ground-based studies often cannot reliably map regions close to the limb, due to telluric seeing, and may therefore miss the highest temperatures observed here at high latitudes at dawn. The spatial morphology of the temperature distribution of Figure 4a has similarities to that of Johnson et al. (2018), with the dawn sector being hotter than the dusk (apart from the DAR), and with a cooler region at the center of the main auroral oval. They also reported a strong correlation between the H_3^+ column density and the observed H_3^+ radiance, which is also seen in this study. Moore et al. (2017) also observed higher temperatures at dawn and the highest H_3^+ column densities at dusk, similar to Wang et al. (2024). The fact that the dawn-side is consistently hotter suggests that this is where the largest Pedersen currents are present, driving strong Joule heating. This is consistent with the increased Pedersen conductances at dawn, compared to dusk, as noted by Rutala, Clarke, et al. (2024).

O'Donoghue et al. (2025) reported high auroral temperatures during a solar wind compression, with dynamic pressures of ~0.6 nPa. The Tao et al. (2005) and Rutala, Jackman, et al. (2024) solar wind propagation models predict the arrival of strong solar wind dynamic pressure in the morning of 2023-09-08, which peaks at ~0.3 nPa, and significantly increased velocity (Figure S2 in Supporting Information S1). Given the relatively large uncertainty in the arrival time (~20 hr), this may be indicative of solar wind driving of the magnetospheric system at the time of the JWST observations, producing a significant increase of the Joule heating in the upper atmosphere and generating elevated temperatures, particularly at polar dawn. The ultraviolet aurora of Jupiter was observed using the HISAKI spacecraft to respond to solar wind compressions with a lag of 10–15 hr, where the solar wind pressure was <0.1 nPa, whilst larger compression did not trigger brighter emissions (Kita et al., 2019), suggesting that the electron precipitation flux did not change significantly. In contrast, the observations of O'Donoghue et al. (2021) showed increased H_3^+ column densities and elevated temperatures during a strong solar wind compression (~0.6 nPa), painting a complex picture of the relationship between ultraviolet H_2 emissions and those of H_3^+, and how these respond to external forcing. Both the UV brightness and the H_3^+ column densities should be sensitive to electron precipitation flux (Tao et al., 2011), whilst the H_3^+ temperature senses predominantly Joule heating (Cowley et al., 2005) and/or changes in the electron energies which sample different parts of the thermospheric temperature profile.

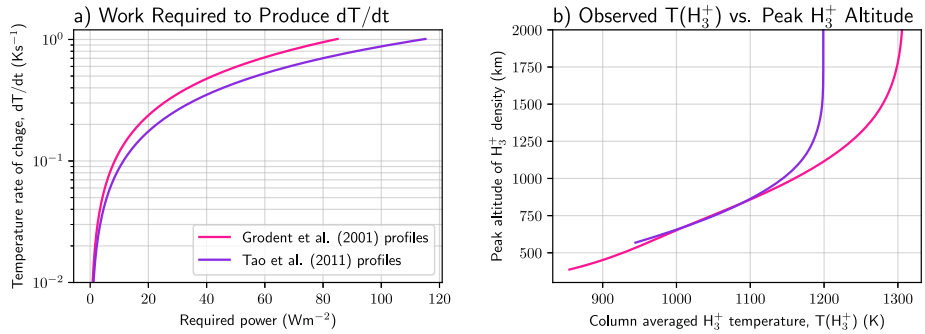

Figure 8. (a) The work required to produce temperature changes in the auroral upper atmosphere of Jupiter, based on the model upper-atmospheric profiles of Grodent et al. (2001) and Tao et al. (2011). The calculation is detailed in Melin et al. (2006). (b) The column averaged H_3^+ temperature weighted by the local H_3^+ density (i.e., the observed H_3^+ temperature) as a function of peak H_3^+ ionospheric altitude.

4.1. Variability

Figure 5c shows the minimum rate of change of temperature, with significant variability observed along and within the main oval. Particularly large changes are seen in the polar-dawn region and at the DAR, which see changes of ∼1 Ks^{-1}. To calculate the power required to physically change the thermal profiles of the upper atmosphere we adopt the same methodology as Melin et al. (2006), using the model auroral atmospheres of Grodent et al. (2001) and Tao et al. (2011). The required power as a function of the rate of change of temperature is shown in Figure 8a. The power required to produce a change of 1 Ks^{-1} is between 85 and 115 Wm^{-2}, depending on the specific model profiles. Using a general circulation model Bougher et al. (2005) derived Joule heating rates of 0.07 Wm^{-2} in the northern auroral region. From Figure 8a, this power input produces heating rates of 6.1 to 8.3 × 10^{-4} Ks^{-1}, which means that it takes ∼25 min to produce a 1 K change in the upper atmosphere. This illustrates that physically altering the temperature profile at Jupiter requires a significant amount of energy that is applied over an extended period of time. Therefore, the fast temperature variations observed here are unlikely to be wholesale changes to the thermospheric temperature structure, and are instead more likely to represent significant changes in the precipitating electron energies: soft electrons will produce H_3^+ at high altitude where the atmosphere is generally hotter, whilst more energetic electrons will produce H_3^+ at lower, cooler, altitudes. Therefore the variability in temperature may be signatures of significant temporal changes in the electron energies. This notion is qualitatively explored, again using the same model vertical profiles used above. The observed line-of-sight H_3^+ temperature is a column average of the local thermospheric temperature, weighted by the local H_3^+ density. By simply shifting the local model H_3^+ density upwards in altitude, and calculating the H_3^+ temperature, we produce a relationship between peak H_3^+ altitude and the H_3^+ temperature, shown in Figure 8b. This shows that elevating the peak H_3^+ density can produce significant changes in the observed H_3^+ temperature. This is because the temperature profiles increases sharply in the lower thermosphere, so that a small change in the peak altitude produces a big change in the observed temperature.

Whilst the observed temperatures are likely related to the electron energies, the rate of change of the H_3^+ column densities (Figure 5d) are instead related to the electron flux, which governs the rate of impact ionization of H_2 required to produce H_3^+. It is also important to note that any changes in the precipitation flux would not be mirrored instantaneously in the H_3^+ column density, but would be smoothed by the chemical lifetime of H_3^+, τ_r, which is given by:

$$\tau_r\left(H_3^+\right) = \frac{1}{\delta(e^-)\kappa_r\left(H_3^+\right)} \tag{5}$$

where $\delta(e^-)$ is the electron density and $\kappa_r\left(H_3^+\right)$ is the recombination rate constant (∼10^{-12} m^3 s^{-1}, Leu et al., 1973). Therefore, as the electron density increases, the lifetime of H_3^+ decreases. The H_3^+ lifetime has been reported to be between 10 and 15 min (Achilleos et al., 1998; Tao et al., 2011), but may also be significantly shorter (∼150 s, Nichols et al., 2025). Since the observed electron densities are highly variable and generally

decrease with altitude (Mendillo et al., 2022), we may also expect the H_3^+ lifetime to be variable within the ionosphere and increase with altitude.

Figure 6 shows the temporal evolution at the NAR and the DAR, as observed in overlapping NIRSpec dithers. Whilst the NAR shows the broad-scale H_3^+ temperature and column density increasing and decreasing in unison ($p = 0.54$), the DAR is highly anti-correlated ($p = -0.81$). This hints that these two regions display very different behaviors. In addition, whilst the density variability is largely similar, the DAR shows much greater variability in temperature, up to 0.6 Ks^{-1} and changes 314 K overall over a period of 39 min. As outlined above, rapid changes in temperature are likely linked to changes in the precipitation energy, which alters the peak production altitude, which in turns impacts the observed H_3^+ temperature (Figure 8b). The fact that the H_3^+ temperature and density are correlated in the NAR and anti-correlated in the DAR suggest that the electron precipitation behaves differently in these two regions. If these changes are solely an altitude effect, then correlated H_3^+ temperature and densities suggest that as the electron energies decrease to sample higher altitudes (i.e., hotter temperatures), the electron flux increases to produce an increase in H_3^+ density, whereas anti-correlated emissions suggest that as electron energies decrease the flux increases.

The fact that the observed H_3^+ temperature in the polar region of Jupiter is determined by both the presence of auroral heating and the altitude at which precipitating electrons deposit their energy presents a dichotomic challenge: how do we differentiate between physical changes to the thermal structure as opposed to just sampling different parts of a (invariable) thermospheric temperature profile? High temperatures are observed along the main auroral oval (Figure 4a) where we also observe high UV color ratios (Figure 7b), indicating hard electrons that penetrate deep that produce H_3^+ just above the homopause, sampling the coldest part of the temperature profile. In this instance, the high temperatures are likely to be driven primarily by auroral Joule heating that has altered the thermal structure. However, the temperatures also vary significantly along the main oval on short time-scales (Figure 5c), which shows that there is strong variability in the precipitating electron energy. In general, temporally averaged temperatures (e.g., Figure 4a) will hide this short-term variability and reveal where heating occurs.

4.2. CH_4 Emissions

Figures 3c and 3d reveals the fine structure of the CH_4 fundamental and hotband emission for the first time. The brightest feature, located at ∼210°W has been observed previously by Juno JIRAM (Moriconi et al., 2017) and by ground-based observatories (e.g., Kim et al., 2015; Kim et al., 2023), and so appears stable over very long time-scales. At around the homopause, where the CH_4 emission emanates from Sánchez-López et al. (2022), the radiative timescales are ∼1 month (Guerlet et al., 2020), whilst at the altitudes that H_3^+ emit, these time scales are likely on the order of <1 hr (Yelle & Miller, 2004). Consequently, the way these two different regions respond to energy inputs may be radically different. If the brightest CH_4 feature in Figure 3c is driven by temperature (Kim et al., 2015), indicating that it is produced via heating, then the observed morphology is a result of temporally averaged auroral heating and stratospheric dynamics and transport. Cavalié et al. (2021) discovered ∼300 ms^{-1} jets in the auroral stratosphere, likely driven by magnetospheric coupling processes, extending deep into the atmosphere (e.g., Sinclair et al., 2023; Wang et al., 2023). It is possible that the combination of long radiative timescales, localized auroral heating in an offset magnetic field, and stratospheric transport interplay to produce the bright CH_4 morphology within the main oval at high latitudes. However, elevated homopause altitudes can also drive enhancements in the CH_4 emissions at 3.3 μm (Sánchez-López et al., 2022). Sinclair et al. (2020) derived elevated homopause altitudes inside the main auroral oval, but did not have spatial resolution nor the spatial coverage close to the pole, where the brightest emissions are observed here. Therefore, the brightest CH_4 3.3 μm emissions may represents where the highest homopause altitude is located within the main auroral oval. To untangle this, further analysis of the data set presented here, as well as from high spatial resolution mid-infrared observations is required, for example, similar to the JWST MIRI analysis of Rodríguez-Ovalle et al. (2024) at Jupiter's southern pole, but for the north.

Figures 3c and 3d also shows fainter CH_4 emissions present along the main auroral oval, suggesting a near instantaneous response to the auroral particle precipitation bombardment. This presents a challenge because of the long radiative time-scales normally associated at the altitudes from which this emission emanates (see above). The non-LTE nature of this emission can significantly reduce these time-scales, activating the CH_4 hotband more quickly in response to energization, compared to the fundamental band. This notion is supported by the CH_4 band

ratio shown in Figure 3b: along the main auroral oval, the fundamental to hotband radiance ratio is ∼2, indicating elevated levels of hotband emissions. This also indicates the degree to which the CH_4 emissions depart from LTE is highly variable across the auroral region. The fundamental CH_4 emissions originate from a lower pressure levels (∼1 μbar) than the hotband emission (∼100 μbar, Sánchez-López et al., 2022). If the non-LTE CH_4 emissions are in part driven by direct excitation by auroral electrons (e.g., Mapstone & Newell, 1994), or their secondaries, then this suggests that very energetic electrons are required to penetrate this deep (several hundreds of keV, Gérard et al., 2014), broadly consistent with the energies along the main oval and in the NAR, derived from Juno UVS observations (Benmahi et al., 2024). However, Bhardwaj and Mukundan (2015) modeled the electron bombardment of CH_4 and found that energies above 50 eV effectively ionizes CH_4, whilst energies less than 10 eV produces vibrational excitation (which is observed here). Therefore, it may be the case that soft energy secondary electrons produce excitation, whilst more energetic electrons initiate ionization and the subsequent complex chain of hydrocarbon chemistry (e.g., Moses et al., 2005). This is conceptually supported by the increased abundances of acetylene seen at the main oval in the southern aurora (Rodríguez-Ovalle et al., 2024).

4.3. Comparisons Between the JWST and Juno UVS

The following discussion must be caveated by the fact that the Juno UVS and JWST observations are not truly simultaneous. The UVS data was acquired between 11:36 and 11:43 on 2023-09-07, whilst the JWST data does not reach auroral latitudes (>50°N) until 13:19, and continues until 16:10 to build up the spatial coverage. Nonetheless, we feel that the multispectral comparison is of value.

The H_3^+ column integrated densities in Figure 4b show significant densities of (up to 1.4×10^{16} m^{-2}) on the dusk region of the planet, with a broad distribution extending from $L = 30$ R_J toward lower L-shells. In general, localized increases in the H_3^+ density requires localized particle precipitation, indicating that the ionization of H_2, which is responsible for the production of H_3^+, occurs in this instance over a broad range of L-shells. In this region the UV H_2 brightness appears diffuse with a relatively low color ratio (Figure 7). This is broadly consistent with the relatively soft broadband electron precipitation that appears omnipresent throughout the auroral region (Salveter et al., 2022). In contrast, the UVS observations show bright emissions on the main oval at around ∼160°W, accompanied by high color ratios. Here, the H_3^+ emissions are very weak (Figure 2b), indicative of a more narrow electron energy distribution that penetrates deep without producing much H_3^+ above the homopause. The H_2 emission morphology and color ratios observed by UVS (albeit with limited spatial coverage) are broadly consistent with those previously observed by the Hubble Space Telescope (e.g., Gustin et al., 2016).

In the NAR region, the UV color ratio is high along with bright H_2 emissions, and patchy emissions are seen in H_3^+. The temporal evolution of the H_3^+ temperature and column density is seen in Figure 6a, showing relatively modest changes in temperature, but larger changes in the density. Again, this is consistent with a variable broadband electron energy distribution that excites and ionizes a large part of the atmospheric column.

The Juno UVS observations show a high color ratio (Figure 7b) along the main oval and at the NAR, which is also where the CH_4 fundamental to hotband band radio is the lowest (Figure 3b), indicating elevated hotband radiances. This suggests that the CH_4 band ratio can be used to trace precipitation depth, in a similar way to the UV color ratio, although detailed modeling would be required to determine the relationship between the observed CH_4 band ratio and precipitating auroral electron energy.

5. Summary

In this study we have presented an analysis of JWST NIRSpec IFU observations of Jupiter's northern auroral region acquired over a range of local times. The averaged view of the H_3^+ aurora show strong emissions along the main oval, but also within it. The highest H_3^+ temperatures are seen at polar-dawn, and these are also the most variable. Significant variability is additionally seen within the DAR region. The peak H_3^+ density is observed equator-ward of the dusk side of the main auroral oval, which is a region associated with low temperature variability. Since this study combines observations obtained over several hours, it is also possible to investigate the temporal variability of the auroral H_3^+ temperatures and column densities. Significant changes (>50%) are seen on time-scales of ∼1 h, which suggests that the energy of the electron precipitation is highly variable, or that the softer electron fluxes sample the sharp gradient in the vertical temperature profile.

The 3.3 μm CH_4 emissions have been mapped at a high spatial resolution with JWST for the first time, showing a bright feature at 210°W at high latitude, which has consistently been observed in the past. There is also significant emission along the main auroral oval, suggesting excitation by direct precipitation, driving these non-LTE emissions. Additionally, the CH_4 fundamental to hotband ratio appears to be associated with precipitation depth within the auroral region. The broad spectral coverage, relatively high resolving power, high spatial resolution offered by JWST offers a powerful new tool with which to investigate the energetics of the aurora at Jupiter, and specifically how this process changes the polar upper atmosphere.

Data Availability Statement

The ground-based image of Jupiter by Yann Le Gall in Figure 1a is available at the Planetary Virtual Observatory and Laboratory: http://pvol2.ehu.eus/pvol2/. The JWST NIRSpec IFU data is available at https://doi.org/10.17909/zp4p-0c93 (Melin, 2024). The `h3ppy` H_3^+ modeling and fitting code is available https://github.com/henrikmelin/h3ppy and Melin (2025b). The projected maps presented here are available at https://doi.org/10.5281/zenodo.16535636 (Melin, 2025a).

Acknowledgments
HM was supported by a STFC James Webb Fellowship (ST/W001527/2) at Northumbria University. TSS and EMT was supported by an STFC Consolidated Grant (ST/Y005325/1) at the Northumbria University. LM acknowledge support by NASA Grant 80NSSC20K1045 issued through the Solar System Workings Program and support from Program number JWST-GO-03665.002-A, which was provided through a grant from the Space Telescope Science Institute under NASA contract NAS5-03127. JO'D. was supported by the STFC Ernest Rutherford Fellowship ST/X003426/1 at the University of Reading. PIT was supported by a STFC studentship. KLK was supported by a Northumbria University Research Studentship. TG was funded by NASA's New Frontiers Program for Juno via contract NNM06AA75C with the Southwest Research Institute. M.L.-P. acknowledges financial support from the Agencia Estatal de Investigación, MCIN AEI/10.13039/501100011033 (Grant PID2022-141216NB-I00 and CEX2021-001131-S). REJ was support by a NERC Grant (NE/W002914/1) at Aberystwyth University. The authors wish to thank two anonymous reviewers for helpful and constructive feedback.

References

Achilleos, N., Miller, S., Tennyson, J., Aylward, A. D., Mueller-Wodarg, I., & Rees, D. (1998). JIM: A time-dependent, three-dimensional model of Jupiter's thermosphere and ionosphere. *Journal of Geophysical Research*, *103*(E9), 20089–20112. https://doi.org/10.1029/98JE00947

Acton, C. H. (1996). Ancillary data services of NASA's navigation and ancillary information facility. *Planetary and Space Science*, *44*(1), 65–70. https://doi.org/10.1016/0032-0633(95)00107-7

Adriani, A., Filacchione, G., Di Iorio, T., Turrini, D., Noschese, R., Cicchetti, A., et al. (2017). JIRAM, the Jovian infrared auroral mapper. *Space Science Reviews*, *213*(1–4), 393–446. https://doi.org/10.1007/s11214-014-0094-y

Badman, S. V., Branduardi-Raymont, G., Galand, M., Hess, S. L. G., Krupp, N., Lamy, L., et al. (2015). Auroral processes at the giant planets: Energy deposition, emission mechanisms, morphology and spectra. *Space Science Reviews*, *187*(1–4), 99–179. https://doi.org/10.1007/s11214-014-0042-x

Benmahi, B., Bonfond, B., Benne, B., Grodent, D., Hue, V., Gladstone, G. R., et al. (2024). Energy mapping of Jupiter's auroral electrons from Juno/UVS data using a new H_2 UV emission model. *A&A*, *685*, A26. https://doi.org/10.1051/0004-6361/202348634

Bhardwaj, A., & Mukundan, V. (2015). Monte Carlo model for electron degradation in methane gas. *Planetary and Space Science*, *111*, 34–43. https://doi.org/10.1016/j.pss.2015.03.008

Bougher, S. W., Waite, J. H., Majeed, T., & Gladstone, G. R. (2005). Jupiter thermospheric general circulation model (JTGCM): Global structure and dynamics driven by auroral and Joule heating. *Journal of Geophysical Research*, *110*(E4), E04008. https://doi.org/10.1029/2003JE002230

Cavalié, T., Benmahi, B., Hue, V., Moreno, R., Lellouch, E., Fouchet, T., et al. (2021). First direct measurement of auroral and equatorial jets in the stratosphere of Jupiter. *A&A*, *647*, L8. https://doi.org/10.1051/0004-6361/202140330

Connerney, J. E. P., Timmins, S., Oliversen, R. J., Espley, J. R., Joergensen, J. L., Kotsiaros, S., et al. (2022). A new model of Jupiter's magnetic field at the completion of Juno's prime mission. *Journal of Geophysical Research: Planets*, *127*(2), e07055. https://doi.org/10.1029/2021JE007055

Cowley, S. W. H., Alexeev, I. I., Belenkaya, E. S., Bunce, E. J., Cottis, C. E., Kalegaev, V. V., et al. (2005). A simple axisymmetric model of magnetosphere-ionosphere coupling currents in Jupiter's polar ionosphere. *Journal of Geophysical Research*, *110*(A11), 11209. https://doi.org/10.1029/2005JA011237

Cowley, S. W. H., & Bunce, E. J. (2001). Origin of the main auroral oval in Jupiter's coupled magnetosphere-ionosphere system. *Planetary and Space Science*, *49*(10–11), 1067–1088. https://doi.org/10.1016/S0032-0633(00)00167-7

Dinelli, B. M., Fabiano, F., Adriani, A., Altieri, F., Moriconi, M. L., Mura, A., et al. (2017). Preliminary JIRAM results from Juno polar observations: 1. Methodology and analysis applied to the Jovian northern polar region. *Geophysical Research Letters*, *44*(10), 4625–4632. https://doi.org/10.1002/2017GL072929

Gérard, J. C., Bonfond, B., Grodent, D., Radioti, A., Clarke, J. T., Gladstone, G. R., et al. (2014). Mapping the electron energy in Jupiter's aurora: Hubble spectral observations. *Journal of Geophysical Research: Space Physics*, *119*(11), 9072–9088. https://doi.org/10.1002/2014JA020514

Gérard, J. C., Mura, A., Bonfond, B., Gladstone, G. R., Adriani, A., Hue, V., et al. (2018). Concurrent ultraviolet and infrared observations of the north Jovian aurora during Juno's first perijove. *Icarus*, *312*, 145–156. https://doi.org/10.1016/j.icarus.2018.04.020

Gladstone, G. R., Persyn, S. C., Eterno, J. S., Walther, B. C., Slater, D. C., Davis, M. W., et al. (2017). The ultraviolet spectrograph on NASA's Juno mission. *Space Science Reviews*, *213*(1–4), 447–473. https://doi.org/10.1007/s11214-014-0040-z

Greathouse, T., Gladstone, R., Versteeg, M., Hue, V., Kammer, J., Giles, R., et al. (2021). Local time dependence of Jupiter's polar auroral emissions observed by Juno UVS. *Journal of Geophysical Research: Planets*, *126*(12), e06954. https://doi.org/10.1029/2021je006954

Grodent, D., Waite, J. H., Jr., & Gérard, J.-C. (2001). A self-consistent model of the Jovian auroral thermal structure. *Journal of Geophysical Research*, *106*, 12933–12952. https://doi.org/10.1029/2000JA900129

Guerlet, S., Spiga, A., Delattre, H., & Fouchet, T. (2020). Radiative-equilibrium model of Jupiter's atmosphere and application to estimating stratospheric circulations. *Icarus*, *351*, 113935. https://doi.org/10.1016/j.icarus.2020.113935

Gustin, J., Grodent, D., Ray, L. C., Bonfond, B., Bunce, E. J., Nichols, J. D., & Ozak, N. (2016). Characteristics of north Jovian aurora from STIS FUV spectral images. *Icarus*, *268*, 215–241. https://doi.org/10.1016/j.icarus.2015.12.048

Jakobsen, P., Ferruit, P., Alves de Oliveira, C., Arribas, S., Bagnasco, G., Barho, R., et al. (2022). The near-infrared spectrograph (NIRSpec) on the James Webb space telescope. I. Overview of the instrument and its capabilities. *A&A*, *661*, A80. https://doi.org/10.1051/0004-6361/202142663

Johnson, R. E., Melin, H., Stallard, T. S., Tao, C., Nichols, J. D., & Chowdhury, M. N. (2018). Mapping H_3^+ temperatures in Jupiter's northern auroral ionosphere using VLT-CRIRES. *Journal of Geophysical Research: Space Physics*, *123*(7), 5990–6008. https://doi.org/10.1029/2018JA025511

Kim, S. J., Sim, C. K., Geballe, T. R., Yung, Y. L., Miller, S., Lee, S., & Tao, C. (2023). Transient energetic particles as the origin of the mid-infrared north polar hotspot of Jupiter. *Icarus*, *398*, 115538. https://doi.org/10.1016/j.icarus.2023.115538

Kim, S. J., Sim, C. K., Ho, J., Geballe, T. R., Yung, Y. L., Miller, S., & Kim, Y. H. (2015). Hot CH_4 in the polar regions of Jupiter. *Icarus*, *257*, 217–220. https://doi.org/10.1016/j.icarus.2015.05.008

Kita, H., Kimura, T., Tao, C., Tsuchiya, F., Murakami, G., Yamazaki, A., et al. (2019). Jovian UV Aurora's response to the solar wind: Hisaki EXCEED and Juno observations. *Journal of Geophysical Research: Space Physics*, *124*(12), 10209–10218. https://doi.org/10.1029/2019JA026997

Lam, H. A., Achilleos, N., Miller, S., Tennyson, J., Trafton, L. M., Geballe, T. R., & Ballester, G. E. (1997). A baseline spectroscopic study of the infrared auroras of Jupiter. *Icarus*, *127*(2), 379–393. https://doi.org/10.1006/icar.1997.5698

Leu, M. T., Biondi, M. A., & Johnsen, R. (1973). Measurements of recombination of electrons with H_3 and H_5^+ ions. *Physical Review A*, *8*(1), 413–419. https://doi.org/10.1103/PhysRevA.8.413

Lystrup, M. B., Miller, S., Stallard, T., Smith, C. G. A., & Aylward, A. (2007). Variability of Jovian ion winds: An upper limit for enhanced Joule heating. *Annales Geophysicae*, *25*(4), 847–853. https://doi.org/10.5194/angeo-25-847-2007

Mapstone, B., & Newell, W. R. (1994). Vibrational excitation of methane by electron impact. *Journal of Physics B: Atomic and Molecular Physics*, *27*(23), 5761–5772. https://doi.org/10.1088/0953-4075/27/23/018

Melin, H. (2024). Data for Jupiter programme #3665 [Dataset]. *STScI/MAST*. https://doi.org/10.17909/zp4p-0c93

Melin, H. (2025a). Derived products for "temporal variability of the northern infrared aurora of Jupiter as captured by JWS" [Dataset]. *Zenodo*. https://doi.org/10.5281/zenodo.16535636

Melin, H. (2025b). h3ppy: An open-source python package for modelling and fitting H_3^+ spectra. *Journal of Open Source Software*, *10*(107), 7536. https://doi.org/10.21105/joss.07536

Melin, H., Miller, S., Stallard, T., Smith, C., & Grodent, D. (2006). Estimated energy balance in the Jovian upper atmosphere during an auroral heating event. *Icarus*, *181*(1), 256–265. https://doi.org/10.1016/j.icarus.2005.11.004

Melin, H., O'Donoghue, J., Moore, L., Stallard, T. S., Fletcher, L. N., Roman, M. T., et al. (2024). Ionospheric irregularities at Jupiter observed by JWST. *Nature Astronomy*, *8*, 1000–1007. https://doi.org/10.1038/s41550-024-02305-9

Melin, H., Stallard, T. S., O'Donoghue, J., Badman, S. V., Miller, S., & Blake, J. S. D. (2014). On the anticorrelation between H_3 temperature and density in giant planet ionospheres. *MNRAS*, *438*(2), 1611–1617. https://doi.org/10.1093/mnras/stt2299

Mendillo, M., Narvaez, C., Moore, L., & Withers, P. (2022). Jupiter's enigmatic ionosphere: Electron density profiles from the pioneer, voyager, and Galileo radio occultation experiments. *Journal of Geophysical Research: Planets*, *127*(3), e07169. https://doi.org/10.1029/2021JE007169

Miller, S., Tennyson, J., Geballe, T. R., & Stallard, T. (2020). Thirty years of H_3^+ astronomy. *Reviews of Modern Physics*, *92*(3), 035003. https://doi.org/10.1103/RevModPhys.92.035003

Moore, L., Melin, H., O'Donoghue, J., Stallard, T. S., Moses, J. I., Galand, M., et al. (2019). Modelling H_3^+ in planetary atmospheres: Effects of vertical gradients on observed quantities. *Philosophical Transactions of the Royal Society of London,Series A*, *377*(2154), 20190067. https://doi.org/10.1098/rsta.2019.0067

Moore, L., O'Donoghue, J., Melin, H., Stallard, T., Tao, C., Zieger, B., et al. (2017). Variability of Jupiter's IR H_3^+ aurorae during Juno approach. *Geophysical Research Letters*, *44*(10), 4513–4522. https://doi.org/10.1002/2017GL073156

Moriconi, M. L., Adriani, A., Dinelli, B. M., Fabiano, F., Altieri, F., Tosi, F., et al. (2017). Preliminary JIRAM results from Juno polar observations: 3. Evidence of diffuse methane presence in the Jupiter auroral regions. *Geophysical Research Letters*, *44*(10), 4641–4648. https://doi.org/10.1002/2017GL073592

Moses, J. I., Fouchet, T., Bézard, B., Gladstone, G. R., Lellouch, E., & Feuchtgruber, H. (2005). Photochemistry and diffusion in Jupiter's stratosphere: Constraints from ISO observations and comparisons with other giant planets. *Journal of Geophysical Research*, *110*(E8), E08001. https://doi.org/10.1029/2005JE002411

Nichols, J. D., Clarke, J. T., Gérard, J. C., Grodent, D., & Hansen, K. C. (2009). Variation of different components of Jupiter's auroral emission. *Journal of Geophysical Research*, *114*(A6), A06210. https://doi.org/10.1029/2009JA014051

Nichols, J. D., King, O. R. T., Clarke, J. T., de Pater, I., Fletcher, L. N., Melin, H., et al. (2025). Dynamic infrared aurora on Jupiter. *Nature Communications*, *16*(1), 3907. https://doi.org/10.1038/s41467-025-58984-z

O'Donoghue, J., Moore, L., Bhakyapaibul, T., Melin, H., Stallard, T., Connerney, J. E. P., & Tao, C. (2021). Global upper-atmospheric heating on Jupiter by the polar aurorae. *Nature*, *596*(7870), 54–57. https://doi.org/10.1038/s41586-021-03706-w

O'Donoghue, J., Moore, L., Melin, H., Stallard, T., Kurth, W. S., Owens, M., et al. (2025). Sub-auroral heating at Jupiter following a solar wind compression. *Geophysical Research Letters*, *52*(7), 2024GL113751. https://doi.org/10.1029/2024GL113751

Raynaud, E., Lellouch, E., Maillard, J.-P., Gladstone, G. R., Waite, J. H., Bézard, B., et al. (2004). Spectro-imaging observations of Jupiter's 2μm auroral emission. I. H_3^+ distribution and temperature. *Icarus*, *171*(1), 133–152. https://doi.org/10.1016/j.icarus.2004.04.020

Roberts, K., Moore, L., O'Donoghue, J., Melin, H., Stallard, T., Knowles, K. L., et al. (2025). Spatiotemporal variations of temperature in Jupiter's upper atmosphere. *The Planetary Science Journal*, *6*(4), 92. https://doi.org/10.3847/PSJ/adc09b

Rodríguez-Ovalle, P., Fouchet, T., Guerlet, S., Cavalié, T., Hue, V., López-Puertas, M., et al. (2024). Temperature and composition disturbances in the southern auroral region of Jupiter revealed by JWST/MIRI. *Journal of Geophysical Research: Planets*, *129*(6), e2024JE008299. https://doi.org/10.1029/2024JE008299

Rutala, M. J., Clarke, J. T., Vogt, M. F., & Nichols, J. D. (2024). Variation in the Pedersen conductance near Jupiter's main emission aurora: Comparison of Hubble space telescope and Galileo measurements. *Journal of Geophysical Research: Space Physics*, *129*(3), e2023JA032122. https://doi.org/10.1029/2023JA032122

Rutala, M. J., Jackman, C. M., Owens, M. J., Tao, C., Fogg, A. R., Murray, S. A., & Barnard, L. (2024). A multi-model ensemble system for the outer heliosphere (MMESH): Solar wind conditions near Jupiter. *Journal of Geophysical Research: Space Physics*, *129*(6), e2024JA032613. https://doi.org/10.1029/2024JA032613

Salveter, A., Saur, J., Clark, G., & Mauk, B. H. (2022). Jovian auroral electron precipitation budget—A statistical analysis of diffuse, mono-energetic, and broadband auroral electron distributions. *Journal of Geophysical Research: Space Physics*, *127*(8), e30224. https://doi.org/10.1029/2021JA030224

Sánchez-López, A., López-Puertas, M., García-Comas, M., Funke, B., Fouchet, T., & Snellen, I. A. G. (2022). The CH_4 abundance in Jupiter's upper atmosphere. *A&A*, *662*, A91. https://doi.org/10.1051/0004-6361/202141933

Seidelmann, P. K., & Divine, N. (1977). Evaluation of Jupiter longitudes in system III (1965). *Geophysical Research Letters*, *4*(2), 65–68. https://doi.org/10.1029/GL004i002p00065

Seiff, A., Kirk, D. B., Knight, T. C. D., Mihalov, J. D., Blanchard, R. C., Young, R. E., et al. (1996). Structure of the atmosphere of Jupiter: Galileo probe measurements. *Science*, *272*(5263), 844–845. https://doi.org/10.1126/science.272.5263.844

Sinclair, J. A., Greathouse, T. K., Giles, R. S., Antuñano, A., Moses, J. I., Fouchet, T., et al. (2020). Spatial variations in the altitude of the CH_4 homopause at Jupiter's mid-to-high latitudes, as constrained from IRTF-TEXES spectra. *The Planetary Science Journal*, *1*(3), 85. https://doi.org/10.3847/PSJ/abc887

Sinclair, J. A., Orton, G. S., Fernandes, J., Kasaba, Y., Sato, T. M., Fujiyoshi, T., et al. (2019). A brightening of Jupiter's auroral 7.8-μm CH_4 emission during a solar-wind compression. *Nature Astronomy*, *3*(7), 607–613. https://doi.org/10.1038/s41550-019-0743-x

Sinclair, J. A., West, R., Barbara, J. M., Tao, C., Orton, G. S., Greathouse, T. K., et al. (2023). Long-term variability of Jupiter's northern auroral 8-μm CH_4 emissions. *Icarus*, *406*, 115740. https://doi.org/10.1016/j.icarus.2023.115740

Stallard, T., Miller, S., Millward, G., & Joseph, R. D. (2002). On the dynamics of the Jovian ionosphere and thermosphere. II. The measurement of H_3^+ vibrational temperature, column density, and total emission. *Icarus*, *156*(2), 498–514. https://doi.org/10.1006/icar.2001.6793

Sulaiman, A. H., Mauk, B. H., Szalay, J. R., Allegrini, F., Clark, G., Gladstone, G. R., et al. (2022). Jupiter's low-altitude auroral zones: Fields, particles, plasma waves, and density depletions. *Journal of Geophysical Research: Space Physics*, *127*(8), e30334. https://doi.org/10.1029/2022JA030334

Tao, C., Badman, S. V., & Fujimoto, M. (2011). UV and IR auroral emission model for the outer planets: Jupiter and Saturn comparison. *Icarus*, *213*(2), 581–592. https://doi.org/10.1016/j.icarus.2011.04.001

Tao, C., Fujiwara, H., & Kasaba, Y. (2009). Neutral wind control of the Jovian magnetosphere-ionosphere current system. *Journal of Geophysical Research*, *114*(A8), A08307. https://doi.org/10.1029/2008JA013966

Tao, C., Kataoka, R., Fukunishi, H., Takahashi, Y., & Yokoyama, T. (2005). Magnetic field variations in the Jovian magnetotail induced by solar wind dynamic pressure enhancements. *Journal of Geophysical Research*, *110*(A11), A11208. https://doi.org/10.1029/2004JA010959

Wang, R., Stallard, T. S., Melin, H., Baines, K. H., Achilleos, N., Rymer, A. M., et al. (2023). Asymmetric ionospheric jets in Jupiter's Aurora. *Journal of Geophysical Research: Space Physics*, *128*(12), e2023JA031861. https://doi.org/10.1029/2023JA031861

Wang, R., Stallard, T. S., Melin, H., Baines, K. H., Moore, L., O'Donoghue, J., et al. (2024). Simultaneous infrared observations of the Jovian auroral ionosphere and thermosphere. *Journal of Geophysical Research: Space Physics*, *129*(12), 2024JA032891. https://doi.org/10.1029/2024JA032891

Yelle, R. V., & Miller, S. (2004). Jupiter's thermosphere and ionosphere. In F. Bagenal, T. E. Dowling, & W. B. McKinnon (Eds.), *Jupiter. The planet, satellites and magnetosphere* (pp. 185–218). Cambridge University Press.